

# Supporting Information for: Capacitive Sensing of Intercalated H<sub>2</sub>O Molecules Using Graphene

Eric J. Olson,<sup>†§</sup> Rui Ma,<sup>†§</sup> Tao Sun,<sup>‡</sup> Mona A. Ebrish,<sup>†</sup> Nazila Haratipour,<sup>†</sup> Kyoungmin Min,<sup>‡</sup>  
Narayana R. Aluru,<sup>‡</sup> and Steven J. Koester<sup>†\*</sup>

<sup>†</sup>*Department of Electrical and Computer Engineering, University of Minnesota-Twin Cities, 200  
Union St. SE, Minneapolis, MN 55455*

<sup>‡</sup>*Department of Mechanical Science and Engineering, Beckman Institute for Advanced Science  
and Technology, University of Illinois at Urbana-Champaign, Urbana, Illinois 61802, USA*  
*\*Ph: (612) 625-1316, FAX: (612) 625-4583, Email: skoester@umn.edu*

<sup>§</sup> *Equal contribution*

### S.1. Metal-oxide-graphene varactor images

Figure S1 shows the optical micrographs of the metal-oxide-graphene (MOG) devices utilized in the experiments. The device utilized for the data shown in Figure 1 of the manuscript had a single gate finger with layout area of  $40 \times 40 \mu\text{m}^2$  and is shown in Figure S1a. The device utilized for the data shown in Figure 3 of the manuscript had 8 gate fingers and had a layout area of  $8 \times 5 \times 40 \mu\text{m}^2$  and is shown in Figure S1b. Finally, the structure utilized to extract the equivalent oxide thickness (EOT) of the  $\text{HfO}_2$  was a metal-insulator-metal (MIM) device shown in Figure S1c. This structure was utilized due to the difficulty in normalizing the area using MOG devices. As we have noted previously,<sup>S1</sup> the active area of the MOG devices could be less than the intended area due to macroscopic and microscopic holes and delamination of the graphene induced either by the transfer process or by etching of the graphene by the ammonium persulfate solution.

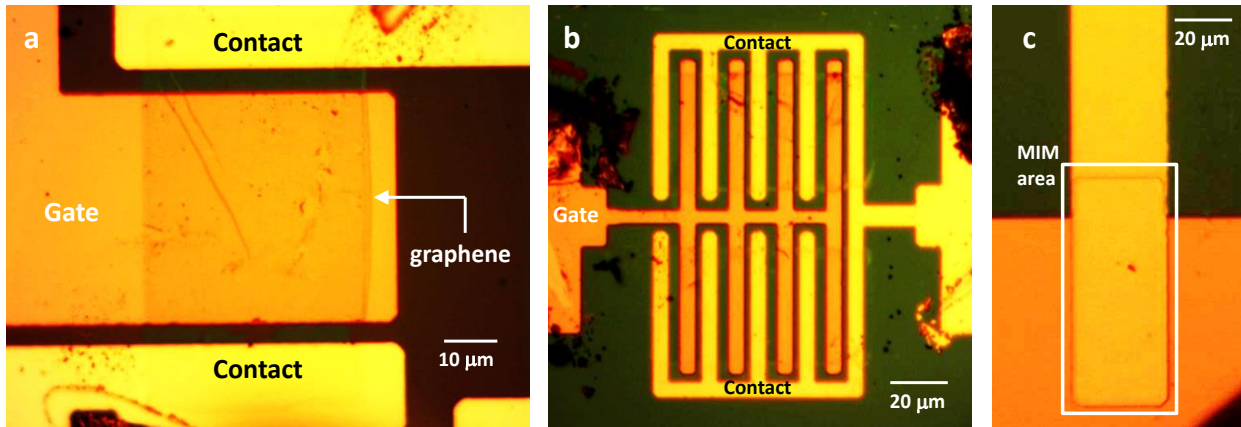


Figure S1. Contrast-enhanced optical micrographs of MOG devices utilized for experiments shown in (a) Figure 1 and (b) Figure 3 of the manuscript, while (c) shows a MIM capacitor utilized to extract the  $\text{HfO}_2$  EOT value.

## S.2. Experimental measurement setup

Figure S2 shows a diagram of the experimental setup utilized for the humidity sensing experiments. While similar to the one utilized in reference S2, the exchange volume of the chamber is significantly smaller, and the chamber also has feedthroughs that allow direct electrical measurement of the device under test (DUT).

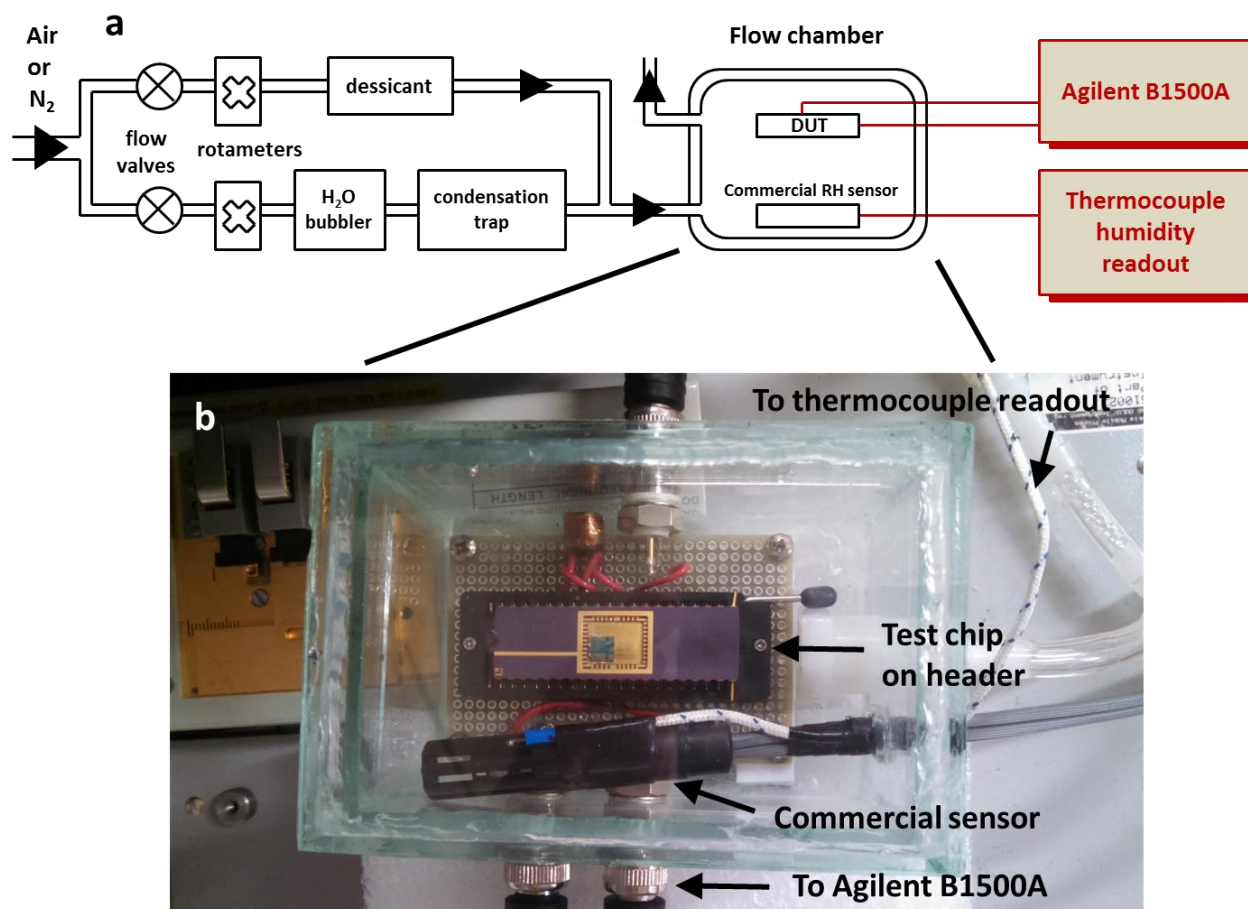


Figure S2. (a) Diagram of humidity sensing measurement setup showing gas flow and electrical feedthroughs. (b) Photograph of the humidity sensing chamber.

## S.3. Variable humidity atomic force microscopy results

Figure S3 shows the additional atomic force microscopy images and thickness histograms utilized to produce the data shown in Figure 2d.

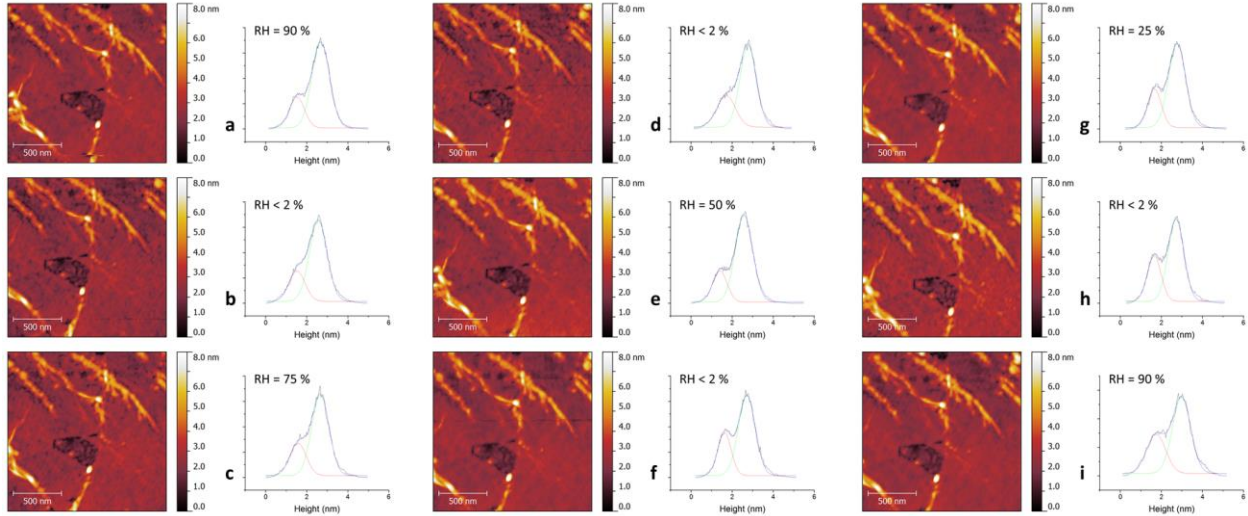


Figure S3. All AFM images from data in Figure 2d for the cases of (a) RH = 90%, (b) RH < 2%, (c) RH = 75%, (d) RH < 2%, (e) RH = 50%, (f) RH < 2%, (g) RH = 25%, (h) RH < 2%, (i) RH = 90%. All the data from (a)-(i) were taken sequentially.

## S.4. Air and nitrogen experiments

### S.4.1. Capacitance-Voltage (*C-V*) characteristics

Typical *C-V* characteristics of the experiments shown in Figure 3 of the manuscript are plotted in Figure S4, and correspond to the data points on the humidity time sequence shown in Figures 3a and 3f. The plot in Figure S4a shows the characteristic of the air experiment at RH = 82.6% and 0.6% (RH decreasing) while the plot in Figure S4b shows the *C-V* curve when RH = 0.4% and 35% (RH increasing). The plot in Figure S4c shows the characteristic of the nitrogen experiment at RH = 74% and 2.8% while the plot in Figure S4d shows the *C-V* curve when RH = 38.4% and 0.25%. At comparable RH values, the Dirac voltage is consistently more positive in air than in nitrogen, suggesting that the oxygen in the air contributes to the p-type doping effect in graphene.

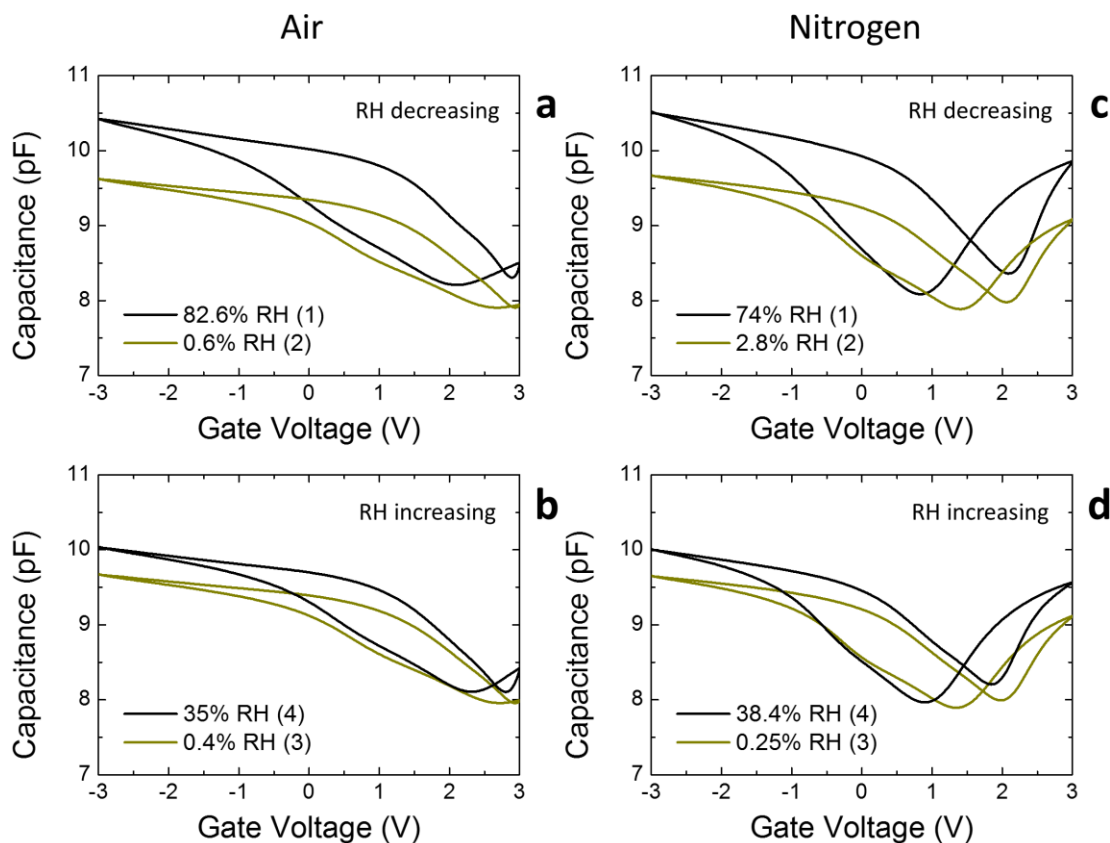


Figure S4. Comparison of MOG C-V characteristics with air (first) and nitrogen (second) as the carrier gas. (a)-(b) Plot of capacitance vs. voltage for a graphene varactor for (a) decreasing relative humidity (RH) and (b) increasing RH, where the plots correspond to the data points on the RH vs. time plot in Figure 3a. (c)-(d) Plot of capacitance vs. voltage for the graphene varactor for (c) decreasing relative humidity (RH) and (d) increasing RH, where the plots correspond to the data points on the RH vs. time plot in Figure 3f.

#### *S.4.2. Reversed order of the air and nitrogen experiments*

We reserved the order of the air and nitrogen humidity sensing experiments in Figure 3 of the manuscript to eliminate effects associated with sensor drift. In this measurement, the nitrogen data was taken before the air experiment. Nitrogen was flowed through the chamber (with the graphene sensor inside) for 24 hours before the measurements shown in Figures S5a-e were performed. Then desiccated air was flowed for 1 hour before the successive experiments in air

(shown in Figures S5f-j) were performed. Figure S5 shows RH,  $C_{\max}$ ,  $C_{\max}/C_{\min}$ ,  $V_{\text{Dirac-avg}}$ , and  $\Delta V_{\text{Dirac}}$  (for both forward and reverse voltage sweeps) vs. time. The general trends are similar to those in Figure 3 of the manuscript, which further confirm the doping effect of oxygen in the air.

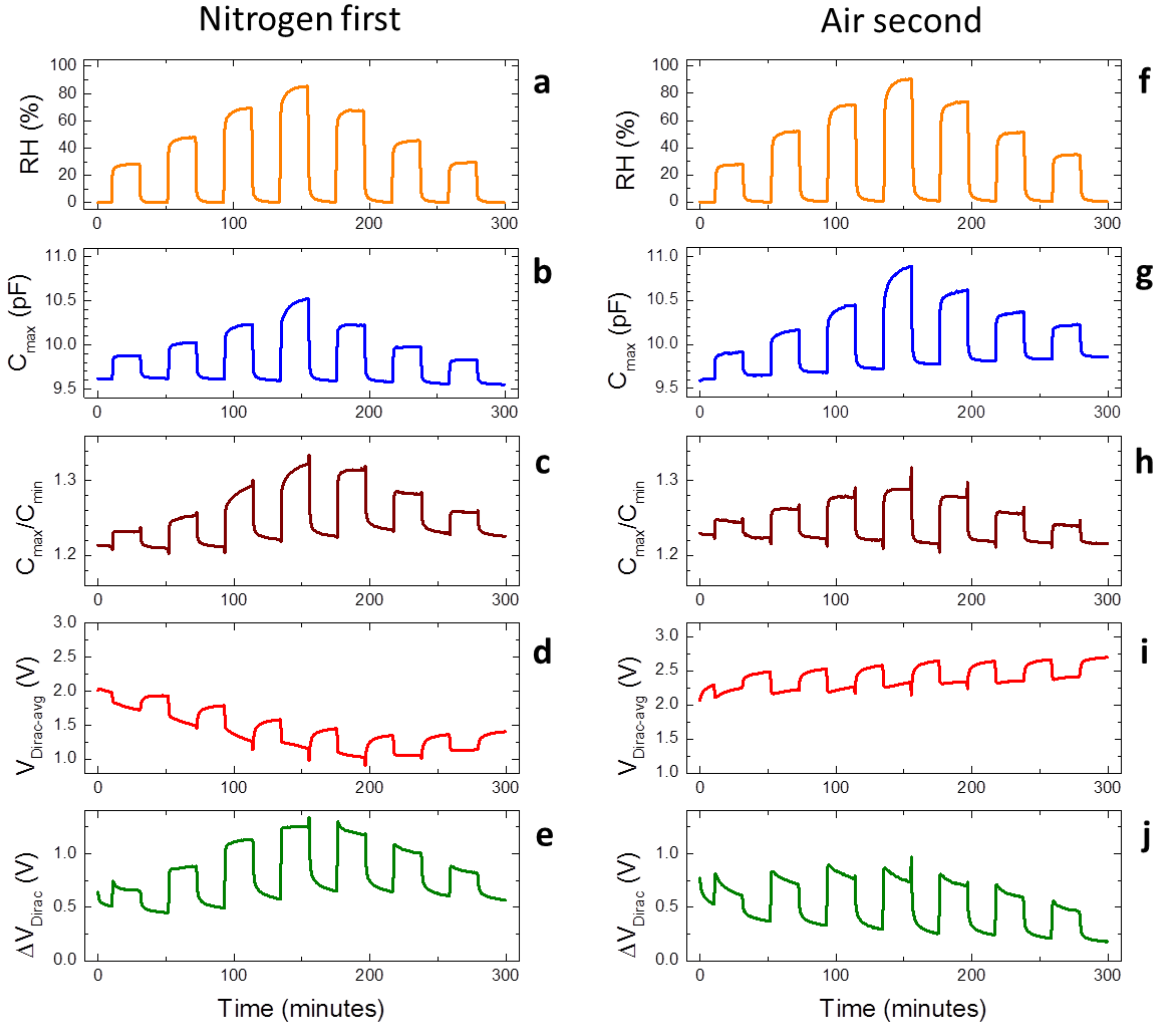


Figure S5. Comparison of MOG humidity sensing characteristics with nitrogen (first) and air (second) as the carrier gas (for the same device in Figure 3). (a) Plot of relative humidity, (b) maximum capacitance,  $C_{\max}$  for forward gate voltage sweep, (c) maximum to minimum capacitance ratio,  $C_{\max}/C_{\min}$  for forward gate voltage sweep, (d) Average Dirac voltage,  $V_{\text{Dirac-avg}}$  between forward and reverse gate voltage sweeps vs. time and (e) The hysteresis,  $\Delta V_{\text{Dirac}}$ , between forward and reverse gate voltage sweeps vs. time with desiccated air as the carrier gas. (f)-(j) Plot of same parameters as in (a)-(e) for same device measured using desiccated air as the carrier gas. The measurements in (a)-(e) were performed first, followed by those in (f)-(j).

## S.5. Oxygen vacancies in HfO<sub>2</sub>

### S.5.1. Number of oxygen vacancies

Oxygen vacancies (VOs) in the HfO<sub>2</sub> surface can induce n-type doping in graphene.<sup>S3</sup> To further understand the effect of change in defect density, the number of VOs is increased from 1 to 4. The location of removed oxygen atoms (atom A, B, C, D) are shown in Figure S6a. First, we obtained the shift of PDOS for graphene as shown in Figure S6b. It indicates that the Fermi Level is further shifted above the Dirac Point (stronger n-type) as more defects are introduced. In addition, interlayer distance and interaction energy between graphene and HfO<sub>2</sub> are calculated and listed in Table S1. More defective sites on HfO<sub>2</sub> induce stronger interaction with graphene surface and hence shorter interlayer distance and stronger interaction energy.

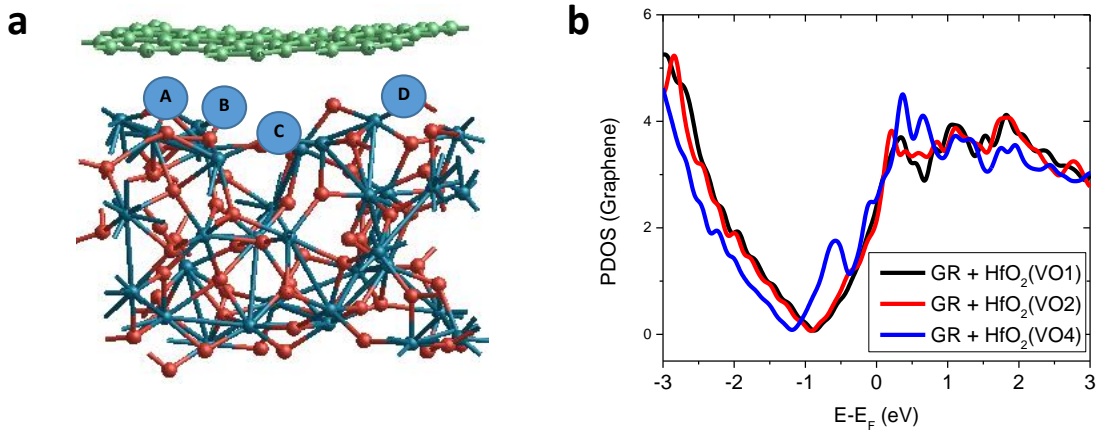


Figure S6. (a) Atomic structure of graphene + HfO<sub>2</sub> with the location of oxygen vacancy (A, B, C, D). (b) PDOS for graphene when the number of oxygen vacancies is increased from 1 (VO1) to 4 (VO4).

**Table S1. Values of ( $E_{\text{Dirac}}-E_{\text{Fermi}}$ ) of graphene, and sub-layer distance and interaction energy between graphene (GR) and HfO<sub>2</sub> (pristine and defective).**

	GR + HfO <sub>2</sub>	GR + HfO <sub>2</sub> (VO1)	GR + HfO <sub>2</sub> (VO2)	GR + HfO <sub>2</sub> (VO4)
$E_{\text{Dirac}}-E_{\text{Fermi}}$ (eV)	0	-0.8745	-0.9205	-1.1929
Interlayer Distance (Å)	2.1122	1.8653	1.8532	1.8292
Interaction Energy (eV)	2.6774	5.9669	6.5639	8.8184

### S.5.2. Hydrogen passivation on oxygen vacancy

To confirm that the n-type doping effect on graphene is from the extra electrons on defective HfO<sub>2</sub> surface, Hf atoms missing O atoms are passivated with H atoms. As shown in Figure S7 PDOS for graphene is recovered to the position where graphene + pristine HfO<sub>2</sub> is located.

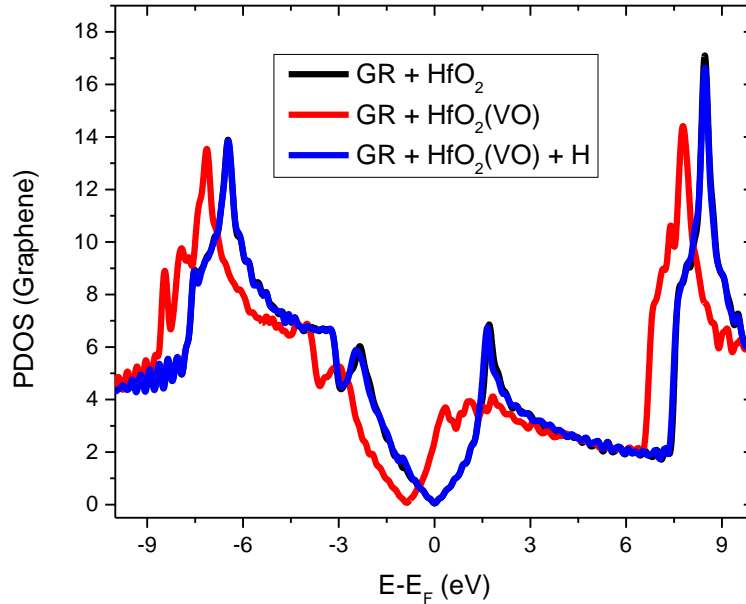


Figure S7. PDOS for graphene interacting with pristine HfO<sub>2</sub>, defective HfO<sub>2</sub>, and hydrogen passivated defective HfO<sub>2</sub>.

### *S.5.3. O<sub>2</sub> effect - bond formation with Hf atom and charge transfer*

When the graphene + HfO<sub>2</sub> (VO) system is exposed to the dry air from vacuum, there is the possibility that O<sub>2</sub> in air can be intercalated between graphene and HfO<sub>2</sub>. Since the defects on HfO<sub>2</sub> surface are reactive sites, O<sub>2</sub> can bond with Hf atoms. To confirm this behavior, we placed O<sub>2</sub> molecules between graphene and HfO<sub>2</sub> surface and relaxed the structure (HfO<sub>2</sub> (VO, O<sub>2</sub>)), shown in Figure S8a, with the location of intercalated O<sub>2</sub> indicated as 1 to 4. It is important to note that the O<sub>2</sub> molecule is attached to Hf atoms, forming Hf-O bonds and so the O<sub>2</sub> saturated device becomes intrinsic, as shown in Figure S8d; that is, the Dirac point of graphene is coincident with its Fermi Level. Also from Figure S8b, we can see the charge redistribution area between graphene and HfO<sub>2</sub> substrate is now very small, which can further confirm that the interaction between graphene and HfO<sub>2</sub> is weaker.

To understand the interaction between the intercalated O<sub>2</sub> and the HfO<sub>2</sub>(VO<sub>4</sub>) substrate, the binding energy between each intercalated O<sub>2</sub> (indicated as 1 to 4 in Figure S8a) and the HfO<sub>2</sub> substrate, together with the bond length between O atoms of intercalated O<sub>2</sub> and Hf atoms on the surface of the HfO<sub>2</sub> substrate were calculated and summarized in Table S2. Figure S8c provides a cartoon view of the results. It should be noted that the average of the binding energies over all Hf-O bonds is ~ 2.50 eV, which is smaller than the reported value of 5.46 eV.<sup>S4</sup> This is consistent with the average value of Hf-O bond lengths (2.179 Å), which is larger than that of the same study, 2.04 Å.<sup>S4</sup> As a result, it is expected that the Hf-O binding energy becomes smaller with increased bond-length. We also performed Bader population analysis<sup>S5-S8</sup> and found the average Bader population for O atoms originally bonded with Hf in HfO<sub>2</sub>(VO<sub>4</sub>) is 7.86638e, while that of those O atoms of the 4 intercalated O<sub>2</sub> molecules is 6.85385e. All of the above show that the

interaction between intercalated  $O_2$  molecules and  $HfO_2(VO_4)$  substrate is weaker than the Hf-O bonds in  $HfO_2$ .

To further understand the effect of  $O_2$  molecules, 5  $O_2$  molecules are placed on the top of graphene +  $HfO_2(VO, O_2)$  and PDOS of graphene is calculated. It shows that  $O_2$  molecules on top accept charge from graphene and hence graphene becomes p-type doped (Figure S8d).

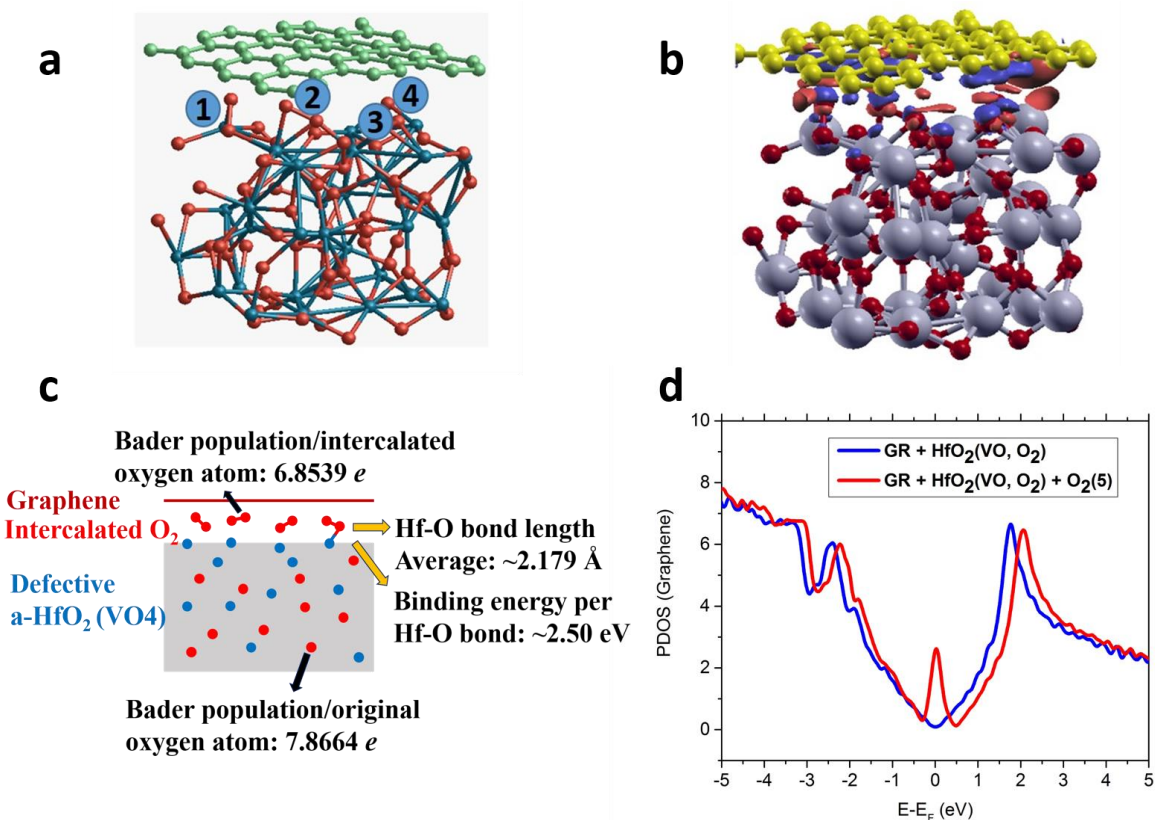


Figure S8. (a) Atomic structure and (b) charge redistribution of the system of graphene (GR) and  $HfO_2$  whose defects (VO) are saturated with  $O_2$  molecules ( $HfO_2(VO, O_2)$ ). (c) Schematic view of the system to show the average Hf-O bond length between O atoms of intercalated  $O_2$  and Hf atoms on the surface of defective  $HfO_2$ , average binding energy per bond and Bader population of intercalated and original O atoms are also shown. (d) PDOS of graphene for the structure of graphene +  $HfO_2(VO, O_2)$  with/without 5  $O_2$  molecules on top.

**Table S2. Binding energies and Hf-O bond-lengths when additional 4 O<sub>2</sub> molecules are attached to surface of defective HfO<sub>2</sub> with 4 O vacancies (Figure S6a).**

Oxygen index	1	2	3	4
Binding energy (eV)	-10.98	-10.02	-11.07	-9.27
Hf-O bond-length (Å)	2.18	2.00	2.16	2.03
	2.18	2.22	2.20	2.05
	2.12	2.15	2.50	2.20
	2.26	--	2.25	--

## S.6. Molecular composition of oxygen and water molecules

### S.6.1. Water molecules between graphene and HfO<sub>2</sub>

When the humidity is increased, experiment results indicate that water molecules can intercalate between graphene and HfO<sub>2</sub> and increase the interlayer distance. To clarify the effect of intercalated water layer, we compare PDOS of graphene for the structure of graphene + HfO<sub>2</sub> + O<sub>2</sub> and H<sub>2</sub>O (top) with and without water layer between graphene and HfO<sub>2</sub>. The structure setups are shown in Figures S9a and S11a. Figure S9c indicates that a layer of water between graphene and HfO<sub>2</sub> does not affect the charge redistribution of graphene; the Dirac point and doping level for both structures are consistent.

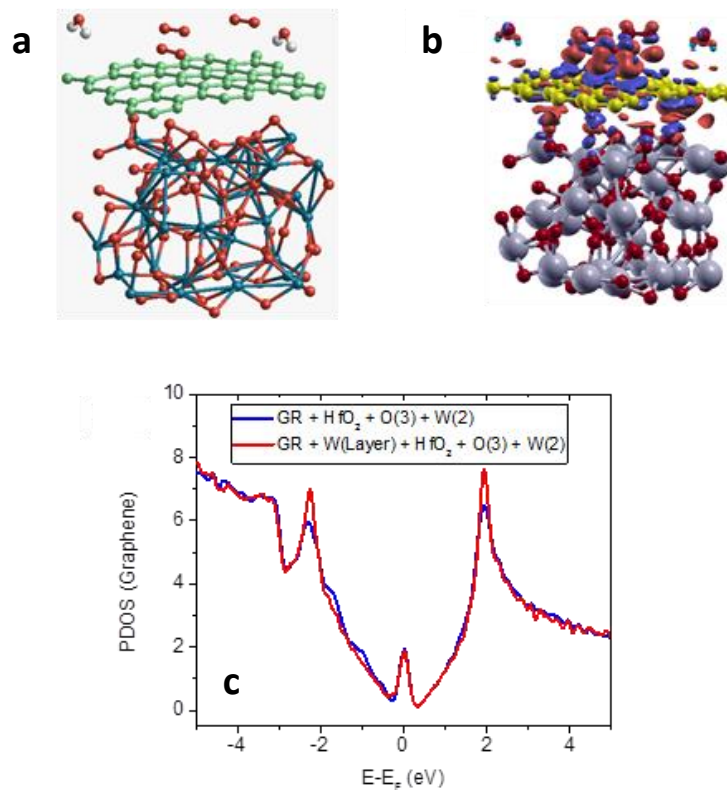


Figure S9. (a) Atomic structure, (b) charge redistribution, and (c) PDOS of graphene for the structure of graphene + HfO<sub>2</sub> + O<sub>2</sub> and H<sub>2</sub>O (top) with and without water layer between two layers.

### *S.6.2. Water and oxygen molecules on top of graphene*

To further understand the effect of increased humidity in experiments, the composition of O<sub>2</sub> and H<sub>2</sub>O molecules on top of graphene is investigated. It is expected that under high humidity, more H<sub>2</sub>O molecules are present above graphene while fewer O<sub>2</sub> molecules exist. To investigate this behavior, we perform MD simulations of O<sub>2</sub> and H<sub>2</sub>O mixture in the confined system.

The simulation box has the dimension of  $100.70 \times 102.09 \times 2230 \text{ \AA}^3$ . We put graphene sheets on both top and bottom of the box with the periodical boundary condition in x- and y-directions. We first introduced 574 O<sub>2</sub> into the box and performed MD simulation with NVT ensemble at 293.15 K. The number of O<sub>2</sub> was determined by matching the bulk density of O<sub>2</sub> at 293.15 K and 1 atm. After the system reached the equilibrium state, we added 347 H<sub>2</sub>O into the

simulation box, mixing with O<sub>2</sub>, and the system was relaxed again. The number of H<sub>2</sub>O added to the system was determined by matching the bulk density of water vapor under the same condition as that of O<sub>2</sub>.

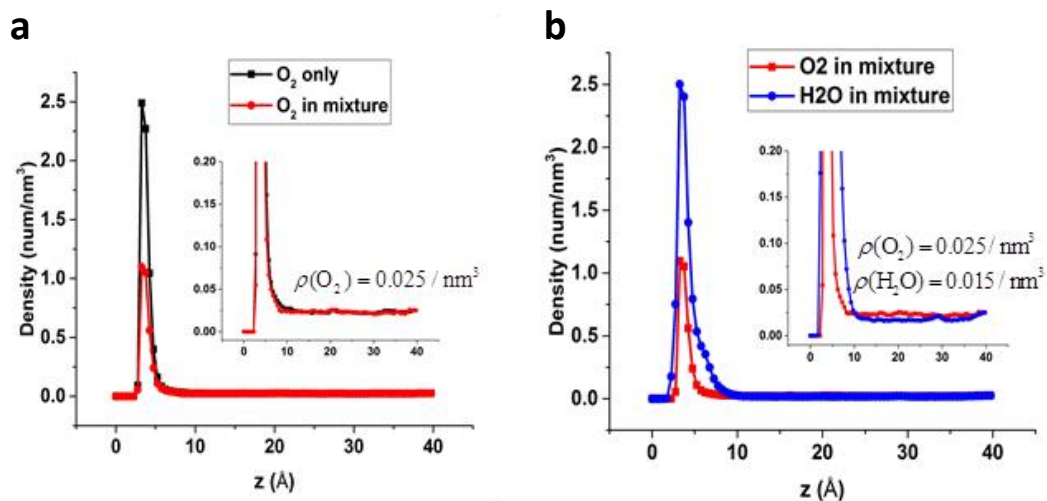


Figure S10. (a) Density profile of O<sub>2</sub> along z-direction for pure O<sub>2</sub> and H<sub>2</sub>O-O<sub>2</sub> mixture, respectively. The subplot is the bulk density of O<sub>2</sub> under 293.15 K and 1 atm. (b) Density profile of O<sub>2</sub> and H<sub>2</sub>O molecules along z-direction for H<sub>2</sub>O-O<sub>2</sub> mixture. The subplot is the bulk density of O<sub>2</sub> and water vapor under 293.15 K and 1 atm.

The density profiles along the z-direction for O<sub>2</sub> and H<sub>2</sub>O molecules are shown in Figures S10a and 10b. From Figure S10a, after H<sub>2</sub>O are added into the system, the first peak of density profile of O<sub>2</sub> drops significantly while the position of the peak remains the same as before. This indicates that there are fewer O<sub>2</sub> above graphene in the mixture than the pure O<sub>2</sub> case. From Figure S10b, in the H<sub>2</sub>O-O<sub>2</sub> mixture, the first peak of density profile of H<sub>2</sub>O is located at the same position as that of O<sub>2</sub>. This means H<sub>2</sub>O molecules are present at nearly the same distance above graphene as O<sub>2</sub>. These results clarify that at higher humidity, H<sub>2</sub>O is present above graphene, and the number of O<sub>2</sub> is smaller compared to the pure O<sub>2</sub> case.

In order to understand graphene doping effect when H<sub>2</sub>O is placed above graphene and correspondingly the number of O<sub>2</sub> is decreased, we performed DFT simulations. We changed the composition from 5 O<sub>2</sub> (W0\_O5) to 4 H<sub>2</sub>O and 1 O<sub>2</sub> (W4\_O1) to investigate the change in doping effect. As expected, W0\_O5 shows the strongest p-type doping effect. Then, as more H<sub>2</sub>O molecules are introduced, the Fermi Level shifts up but still below the Dirac Point (less p-type effect) and the density of extra electron hole energy levels at 0 eV is decreased. (Figure S11b)

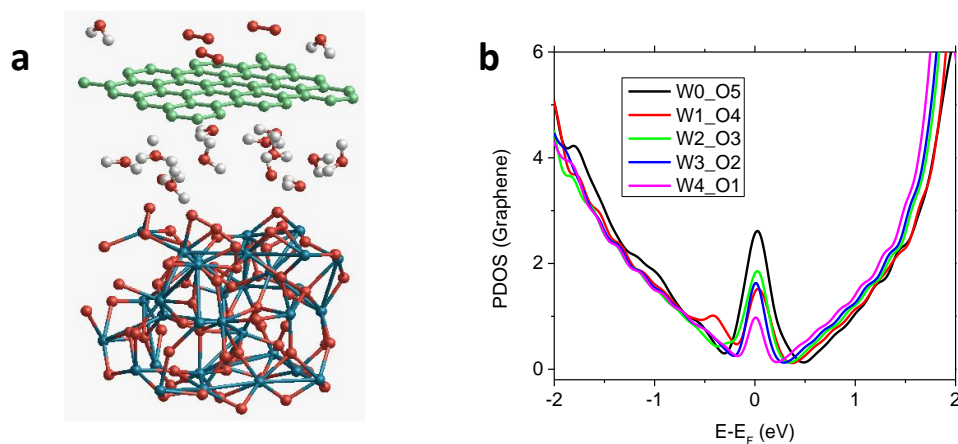


Figure S11. (a) Atomic structure and (b) PDOS for graphene from the structure of water and oxygen mixture + graphene + water layer + HfO<sub>2</sub> with different composition of H<sub>2</sub>O and O<sub>2</sub> molecules

### S.7. Bader population with different exchange-correlation (XC) functionals.

In the main manuscript, we calculated Bader population<sup>S5-S8</sup> for graphene sheets in different systems to understand graphene doping effect. Since Bader population can be dependent on exchange-correlation (XC) functionals, Bader population analysis for the systems in Figure 4a to 4d in the manuscript was performed using different functionals. For generalized gradient approximation (GGA), we used Perdew-Burke-Ernzerhof (PBE),<sup>S9</sup> Perdew-Burke-Ernzerhof for solids (PBEsol),<sup>S 10</sup> and Revised Perdew-Burke-Ernzerhof (RPBE)<sup>S 11</sup> functionals. For local

density approximation (LDA), we used Ceperley-Alder (CA)<sup>S12</sup> and Perdew-Wang-92 (PW92)<sup>S13</sup> functionals. The results are listed in Table S3. It should be noted that Bader population analysis shows negligible dependency on different XC functions.

**Table S3. Bader population calculation for systems from (a) to (d) in Figure 4 with different exchange-correlation functionals.**

Bader population ( $e$ )	Structure			
	a	b	c	d
GGA_PBE	191.9625	196.0929	191.3996	191.6643
GGA_PBEsol	191.9637	196.1519	191.4439	191.6974
GGA_RPBE	191.9603	196.0666	191.402	191.6662
LDA_CA	191.9624	196.1669	191.4237	191.6826
LDA_PW92	191.9622	196.1658	191.4218	191.6815

### S.8. Donor State near the Fermi Level of Graphene

It should be noted that in Figure 5a of the manuscript, when O<sub>2</sub> molecules are adsorbed on the surface of graphene, there is a small peak near the Fermi Level of graphene in the PDOS plot, indicating the appearance of additional states. Here, we provide an explanation of this behavior. Consider the system in Figure S12a in which an O<sub>2</sub> molecule is adsorbed on top of graphene. After structure relaxation we obtain the band structure of the whole system and the PDOS of graphene, shown in Figures S12b and S12c. For the band structure, there are two states near the Fermi Level which are not present in the pure graphene system. Also for PDOS of graphene, there is a small peak appearing at the Fermi Level. The wave functions (plotted using the VESTA program<sup>S14</sup>) corresponding to the four states near the Fermi Level (indicated by index 1

to 4) at the  $\Gamma$  point are plotted. The wave functions of state 1 and 4 are located only around graphene while the wave functions of state 2 and 3 are located around both graphene and the  $O_2$  molecule. When the band structure is projected to the carbon atoms to obtain the PDOS of graphene, state 2 and 3 also have contributions to the PDOS, thus a peak appears near the Fermi Level of graphene in the PDOS plot.

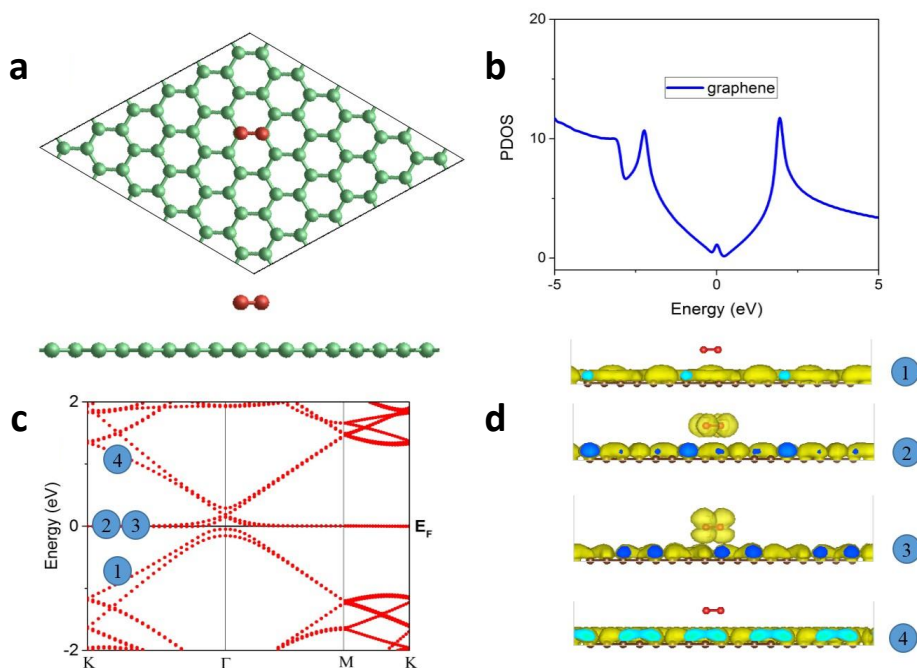


Figure S12. (a) Atomic structure and (b) band structure for graphene with an  $O_2$  molecule adsorbed on top. (c) PDOS of graphene, the Fermi Level is adjusted to be 0 eV. (d) Plot for wave functions of the 4 states in (b).

### S.9. Video of Molecular Dynamics Simulations

A video of the entire intercalation process is provided in the video at the following link:

[MD\\_intercalation.avi](#)

## References

- S1 Ebrish, M.A., & Koester, S. J. Dielectric Thickness Dependence of Quantum Capacitance in Graphene Varactors with Local Metal Back Gates, *Proc. 70<sup>th</sup> Dev. Res. Conf. (DRC)*, 105-106 (2012).
- S2 Deen, D. A., Olson, E. J., Ebrish, M. A. & Koester, S. J. Graphene-based Quantum Capacitance Wireless Vapor Sensors. *IEEE Sensors J.* **14**, 1459-1466 (2014).
- S3 Scopel, W., Fazzio, A., Miwa, R. & Schmidt, T. Graphene on Amorphous HfO<sub>2</sub> Surface: An *ab initio* Investigation. *Phys. Rev. B* **87**, 165307 (2013).
- S4 Hou, Z. F., Gong, X. G., & Li, Q. Energetics and Electronic Structure of Aluminum Point Defects in HfO<sub>2</sub>: A First-Principles Study. *J. Appl. Phys.* **106**, 014104 (2009).
- S5 Henkelman, G., Arnaldsson, A. & Jónsson, H. A Fast and Robust Algorithm for Bader Decomposition of Charge Density. *Computational Materials Science* **36**, 354-360 (2006).
- S6 Sanville, E., Kenny, S. D., Smith, R. & Henkelman, G. Improved Grid-based Algorithm for Bader Charge Allocation. *Journal of Comp. Chem.* **28**, 899-908 (2007).
- S7 Tang, W., Sanville, E. & Henkelman, G. A Grid-based Bader Analysis Algorithm without Lattice Bias. *Journal of Physics: Condensed Matter* **21**, 084204 (2009).
- S8 Perdew, J. P., Burke, K. & Ernzerhof, M. Generalized Gradient Approximation Made Simple. *Phys. Rev. Lett.* **77**, 3865-3868 (1996).
- S9 Perdew, J. P., Burke, K. & Ernzerhof, M. Generalized Gradient Approximation Made Simple. *Phys. Rev. Lett.* **77**, 3865-3868 (1996).
- S10 Perdew, J. P. *et al.* Restoring the Density-Gradient Expansion for Exchange in Solids and Surfaces. *Phys. Rev. Lett.* **100**, 136406 (2008).
- S11 Hammer, B., Hansen, L. B. & Nørskov, J. K. Improved Adsorption Energetics within Density-Functional Theory Using Revised Perdew-Burke-Ernzerhof Functionals. *Phys. Rev. B* **59**, 7413 (1999).
- S12 Perdew, J., McMullen, E. & Zunger, A. Density-Functional Theory of the Correlation Energy in Atoms and Ions: A Simple Analytic Model and a Challenge. *Phys. Rev. A* **23**, 2785 (1981).
- S13 Perdew, J. P. & Wang, Y. Accurate and Simple Analytic Representation of the Electron-gas Correlation Energy. *Phys. Rev. B* **45**, 13244 (1992).
- S14 Momma, K. & Izumi, F. VESTA 3 for Three-dimensional Visualization of Crystal, Volumetric and Morphology Data. *J. Appl. Crystallogr.* **44**, 1272-1276 (2011).